

Generation of polarization-entangled optical coherent waves and manifestation of vector singularity patterns

T. H. Lu, Y. F. Chen, and K. F. Huang

Department of Electrophysics, National Chiao Tung University, Hsinchu, Taiwan

(Received 6 December 2006; published 27 February 2007)

We use a high-level isotropic laser with off-axis focused and on-axis circular pumping to generate the high order polarization-entangled transverse modes. The main finding is that the complex transverse modes can be categorized into four types: square pattern, hyperbolic pattern, elliptic pattern, and circular pattern. Importantly, all types of the polarization-entangled modes can be well analyzed with the generalized coherent states. With the connection between theoretical analysis and experimental results, the formation of complex singularities can be clearly represented.

DOI: [10.1103/PhysRevE.75.026614](https://doi.org/10.1103/PhysRevE.75.026614)

PACS number(s): 42.25.Ja, 02.40.Xx, 03.65.Vf

I. INTRODUCTION

Over the past few years a considerable number of studies have been made on the coherent wave properties in mesoscopic physics. Much research has been focused on phase singularities in scalar fields, known as wave front dislocations, such as quantum ballistic transport [1], vortex lattices in superconductors [2], quantum Hall effects [3], linear and nonlinear optics [4,5], and Bose-Einstein condensates [6,7]. In recent years, polarization singularities, known as wave front disclinations, are also noticed in modern physics [8–10]. As mentioned by Freund [11], there are two types of singularities of the polarization vectors of paraxial optical beams: vector singularities and Stokes singularities. Vector singularities are isolated, stationary points in a plane at which the orientation of the electric vector of a linearly polarized vector field becomes undefined. The nature of the vector singularities has been studied in the coherent optical waves with the correlated behavior of spatial structures and polarization states [12–15].

Recently, a microchip solid-state laser has been employed to perform analogous studies of the coherent scalar waves in the quantum-classical correspondence [16]. Furthermore, an isotropic microchip laser has been used to generate the polarization vector field that is made up of two linearly polarized modes with different spatial structures that are phase synchronized to a single frequency [17]. However, the high-order polarization-entangled transverse modes are found to lack the flexibility because of the doughnut pump profile. Nowadays, manipulation and generation of the polarization-entangled optical wave may be promising for some fundamental investigations, such as light-matter interaction.

In this work we demonstrate two practical pump schemes to generate various kinds of polarization-entangled patterns. One of the schemes is the off-axis focused pump profile, and the other is the on-axis circular pump profile. With these two pumping schemes, we can generate various kinds of polarization-entangled patterns in the highly isotropic resonator. Experimental results reveal that the polarization-entangled transverse modes can be categorized into four types: square pattern, hyperbolic pattern, elliptic pattern, and circular pattern. All types of the polarization-entangled patterns can be analytically reconstructed with the generalized

coherent states. With the connection between theoretical analysis and experimental results, the formation of complex singularities can be clearly represented.

II. EXPERIMENTAL SETUP AND RESULTS

In the experiment, the laser system is a diode-pumped Nd:YVO₄ microchip laser and the resonator configuration is depicted in Fig. 1. The laser gain medium was a c-cut 2.0-at. % Nd:YVO₄ crystal with a length of 2 mm. One side of the Nd:YVO₄ crystal was coated for partial reflection at 1064 nm. The radius of curvature of the cavity mirror is $R = 10$ mm and its reflectivity is 99.8% at 1064 nm. The pump source was an 809 nm fiber-coupled laser diode with a core diameter of 100 μm , a numerical aperture of 0.16, and a maximum output power of 1 W. A focusing lens with 20 mm focal length and 90% coupling efficiency was used to reimage the pump beam into the laser crystal. Since the YVO₄ crystal belongs to the group of oxide compounds crystallizing in a zircon structure with tetragonal space group, the Nd-doped YVO₄ crystals show strong polarization dependent fluorescence emission due to the anisotropic crystal field. The fourfold symmetry axis of the YVO₄ crystal is the crystallographic c axis; perpendicular to this axis are the two indistinguishable a and b axes. Therefore, the Nd:YVO₄ crystal is precisely cut along the c axis for high-level transverse isotropy. It is practical to note that our gain medium is

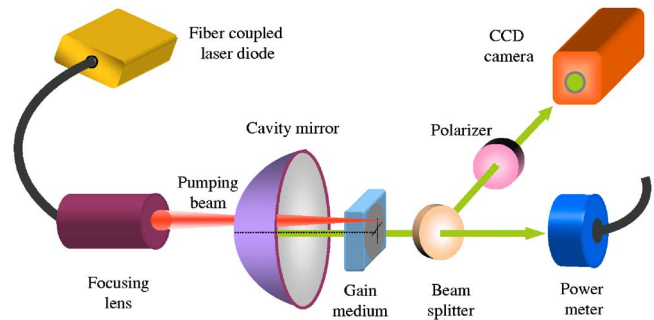


FIG. 1. (Color online) Experimental setup for the generation of polarization-entangled transverse modes with off-axis pumping scheme in a highly isotropic diode-pumped microchip laser.

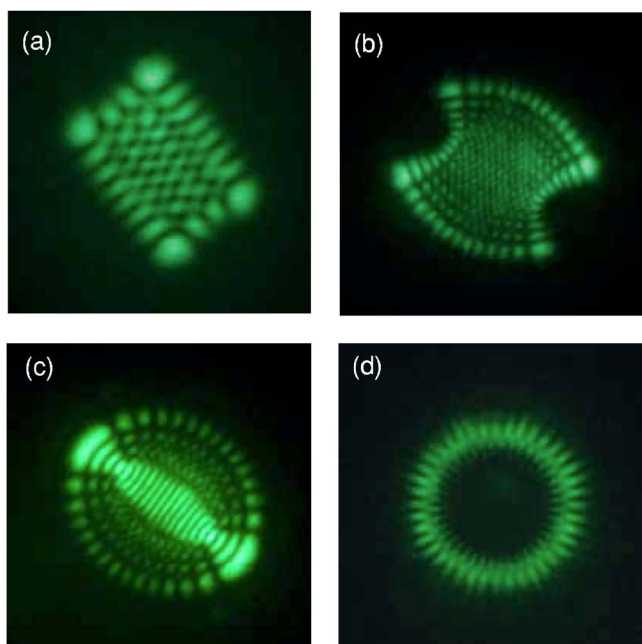


FIG. 2. (Color online) Experimental polarization-entangled patterns (a) square pattern, (b) hyperbolic pattern, (c) elliptic pattern, (d) circular pattern.

different from the conventional Nd:YVO₄ crystals that are cut along the a axis to use the largest stimulated emission cross section for lowering the lasing threshold. To measure the transverse far-field pattern, the output beam was directly projected into the CCD camera. Figure 1 shows the scheme of the highly isotropic laser system in this work.

First of all, we demonstrate that the off-axis focused configuration can be used to generate the three kinds of polarization-entangled patterns: square pattern, hyperbolic pattern, and elliptic pattern which are shown in Figs. 2(a)–2(c). With controlling the pump position (x_0, y_0) with respect to the propagation axis, the square, hyperbolic, and elliptic patterns can be generated. The pump positions are at $(-50 \mu\text{m}, 63 \mu\text{m})$, $(-140 \mu\text{m}, 20 \mu\text{m})$, and $(-137 \mu\text{m}, 61 \mu\text{m})$ for the square, hyperbolic, and elliptic patterns, respectively. Note that the radial distance of the pumping beam $r_0 = \sqrt{x_0^2 + y_0^2}$ determines the lasing mode size. The radial distances of pumping beam for the square, hyperbolic, and elliptic pattern are 80, 140, and 150 μm , respectively, which are consistent with the mode sizes of the three experimental transverse modes. Off-axis pumping is employed to generate the polarization-entangled states which are respectably stable with highly isotropic laser system. Figure 2(d) shows the circular pattern which can be generated with the on-axis defocused pump scheme. The on-axis pumping provides a good symmetry to generate the stable circular modes. It can be seen that the formation of the stationary polarization-entangled mode is primarily dependent on the overlap between the pump intensity and the lasing mode distribution. This is consistent with the fact that the cavity mode with the biggest overlap of the gain region will dominate the lasing process. In other words, controlling the pumping scheme and the pumping position can precisely manipulate the generation of various stationary polarization-entangled modes in a

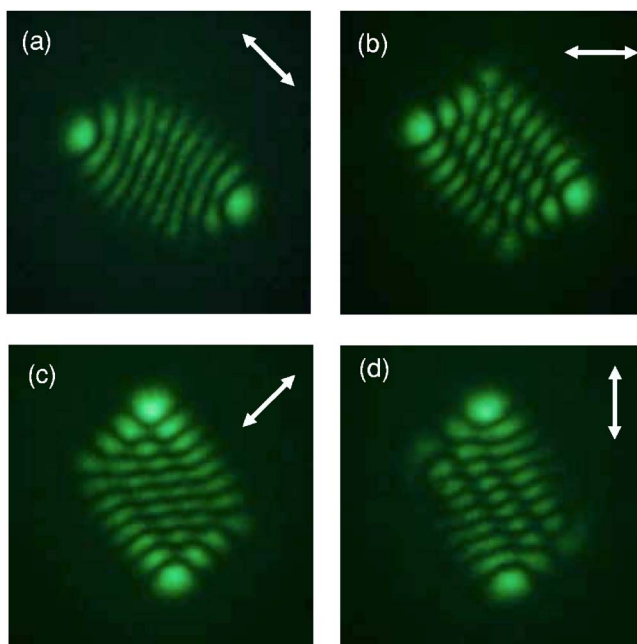


FIG. 3. (Color online) Experimental polarization-resolved patterns according to the pattern in Fig. 2(a). (a) 45° polarization, (b) 90° polarization, (c) 135° polarization, (d) 180° polarization.

highly isotropic laser cavity. All of the experimental modes are preserved from the near-field to the far-field patterns because they are found to be coherently superposed by the transverse modes with the same Gouy phase.

All the lasing modes are found to be made up of two distinct patterns with orthogonal linear polarization. That is to say, the polarization of the transverse pattern is linear but spatially dependent. Figures 3–6 show the experimental polarization-resolved patterns in the 45°, 90°, 135°, and 180° direction according to the patterns in Figs. 2(a)–2(d). It is found that the entanglement of the spatial structures and polarization states forms an optical vector field and leads to the transverse patterns to be polarization dependent. Although the structures of the polarization-entangled patterns are complex, the lasing modes are quite stable and easily reproducible with the present pumping schemes. It is worthwhile to mention that the basic requirement for the formation of a vector polarization pattern is that the orthogonal polarization modes with different spatial patterns are phase synchronized to a common frequency. The measurement of the optical spectrum is used in the experiment to verify the polarization-resolved pattern to be phase synchronized to a single frequency.

III. ANALYTICAL WAVE FUNCTIONS FOR EXPERIMENTAL POLARIZATION-ENTANGLED PATTERNS

The wave function for the paraxial field in the spherical laser resonator can be expressed as Hermite-Gaussian (HG) function with Cartesian symmetry $\Phi_{m,n}^{HG}(x, y, z)$, where m and n are the indices of x and y coordinates or Laguerre-Gaussian (LG) function with cylindrical symmetry $\Phi_{p,l}^{LG}(r, \phi, z)$, where

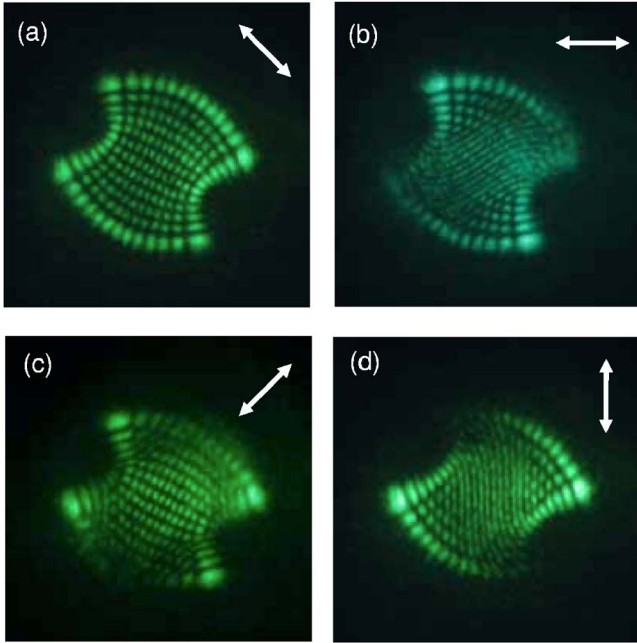


FIG. 4. (Color online) Experimental polarization-resolved patterns according to the pattern in Fig. 2(b). (a) 45° polarization, (b) 90° polarization, (c) 135° polarization, (d) 180° polarization.

p and l are the radial and azimuthal indices [18]. It is well known that the paraxial wave equation for the spherical resonator has the identical form with the Schrödinger equation for the two-dimensional (2D) harmonic oscillator [18]. The SU(2) coherent states for the 2D harmonic oscillator are well localized on classical elliptic trajectories [19,20]. The SU(2) coherent states have been shown to play an important role for the quantum-classical connection in the 2D quantum sys-

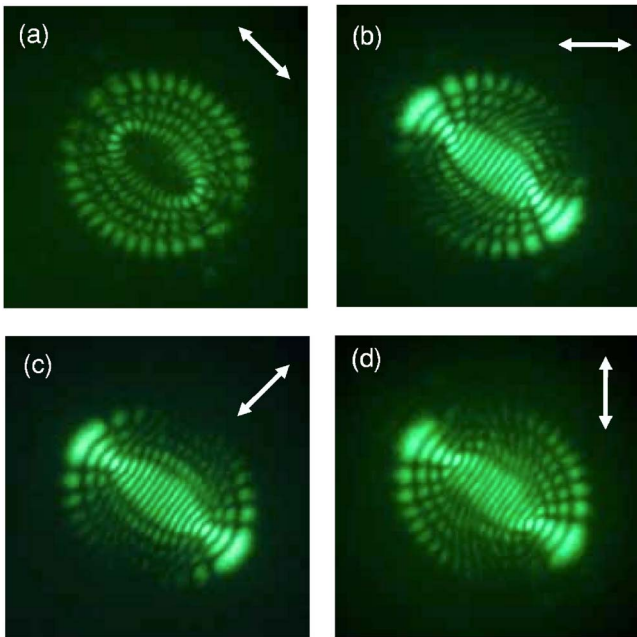


FIG. 5. (Color online) Experimental polarization-resolved patterns according to the pattern in Fig. 2(c). (a) 45° polarization, (b) 90° polarization, (c) 135° polarization, (d) 180° polarization.

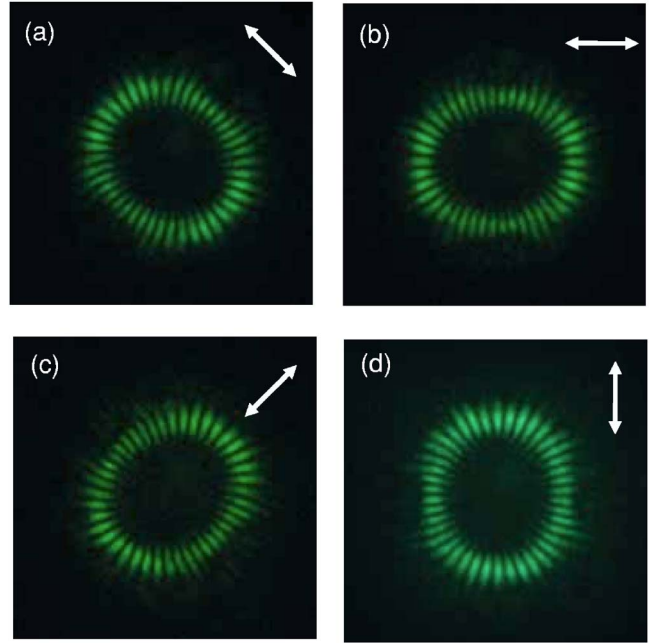


FIG. 6. (Color online) Experimental polarization-resolved patterns according to the pattern in Fig. 2(d). (a) 45° polarization, (b) 90° polarization, (c) 135° polarization, (d) 180° polarization.

tems [21,22]. It has also been confirmed that the experimental elliptic patterns agree very well with the SU(2) elliptic states [23,24]. Even so, the SU(2) coherent states can only be used to describe the elliptic patterns. To explain other polarization-entangled patterns, we need to use the generalized coherent states (GCSs) to be related to the transition from HG modes $\Phi_{m,n}^{HG}(x,y,z)$ into various experimental modes with different phase factor. The GCSs used in this work are identical to those used previously [17]. Here we present a brief synopsis for completeness. In terms of the HG modes, the SU(2) coherent states for the elliptic modes are expressed as [19,20]

$$\Psi_N^{\text{CS}}(x,y,z;\varphi) = \frac{1}{\sqrt{2^N}} \sum_{K=0}^N \frac{\sqrt{N!}}{\sqrt{(N-K)!K!}} e^{iK\varphi} \Phi_{N-K,K}^{HG}(x,y,z), \quad (1)$$

where the parameter φ is the relative phase between various HG modes and is related to the eccentricity of the elliptic trajectory, and the wave function of HG mode is given by

$$\Phi_{m,n}^{HG}(x,y,z) = \frac{1}{\sqrt{2^{m+n-1} \pi m! n!}} \frac{1}{w(z)} H_m \left[\frac{\sqrt{2}x}{w(z)} \right] H_n \left[\frac{\sqrt{2}y}{w(z)} \right] \times \exp \left[-\frac{x^2 + y^2}{w(z)^2} \right], \quad (2)$$

where $w(z) = w_0 \sqrt{1 + (z/z_R)^2}$, w_0 is the beam radius at the waist, and z_R is the Rayleigh range. As shown in a variety of integrable 2D quantum billiard systems, the phase factor φ in the SU(2) coherent states plays a vital role in the quantum-classical connection [21,22]. Any LG modes $\Phi_{p,l}^{LG}(r,\phi,z)$ can be decomposed into a sum of HG modes $\Phi_{2p+l-k,k}^{HG}(x,y,z)$

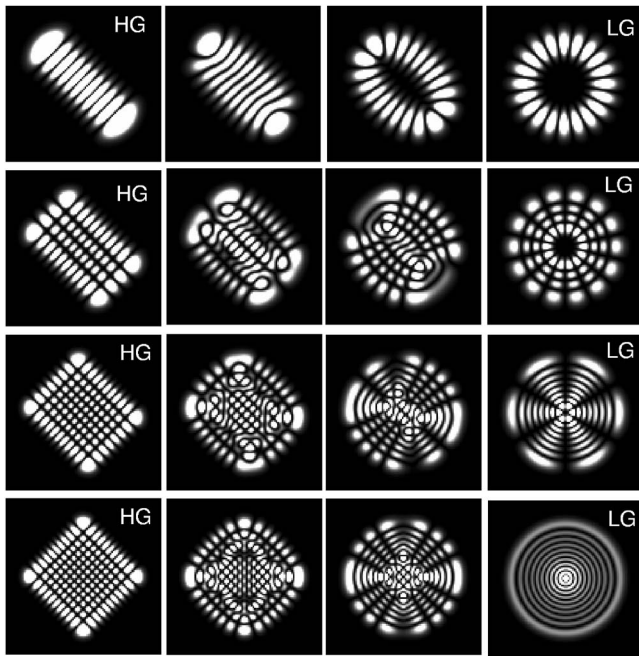


FIG. 7. Numerical patterns of the GCSs with different phase factor and different order. The phase factors of the GCSs from the first to last column are 0 , $\pi/6$, $\pi/3$, and $\pi/2$, respectively; the indices (p, l) from the first to last row are $(0, 10)$, $(3, 7)$, $(7, 3)$, and $(10, 0)$, respectively.

with the same coefficients $B(p, l, k)$ but an additional $\pi/2$ phase factor:

$$\Phi_{p,l}^{LG}(r, \phi, z) = \sum_{k=0}^{2p+l} e^{ik(\frac{\pi}{2})} B(p, l, k) \Phi_{2p+l-k,k}^{HG}(x, y, z) \quad (3)$$

with

$$B(p, l, k) = \frac{(-1)^k}{\sqrt{2^{2p+l}}} \sum_s \frac{(-1)^s \sqrt{(p+l)! p! (2p+l-k)! k!}}{s! (k-s)! (p+l-s)! (p-k+s)!}, \quad (4)$$

where the summation over s is taken whenever none of the argument of factorials in the denominator are negative. As in the representation of $SU(2)$ coherent states, we utilize the phase factor φ to characterize a new family of GCSs:

$$\Psi_{p,l}^{CS}(x, y, z, \varphi) = \sum_{k=0}^{2p+l} e^{i\varphi k} B(p, l, k) \Phi_{2p+l-k,k}^{HG}(x, y, z). \quad (5)$$

The GCSs in Eq. (5) exhibit a traveling-wave property. The standing-wave representation of GCSs is given by

$$\begin{Bmatrix} \Psi_{p,l}^{\cos} \\ \Psi_{p,l}^{\sin} \end{Bmatrix} = \sqrt{2} \begin{bmatrix} \sum_{k=0}^{2p+l} \left\{ \cos(k\varphi) \right\} \\ \sum_{k=0}^{2p+l} \left\{ \sin(k\varphi) \right\} \end{bmatrix} B(p, l, k) \Phi_{2p+l-k,k}^{HG}(x, y, z). \quad (6)$$

The GCSs represent a general family to comprise the HG and LG mode families as special cases. As shown in Fig. 7, it exhibits that the phase factor φ plays an important role for the GCSs to transform from the HG modes to the LG modes

in different order. On the one hand the GCSs represent to the HG modes when the phase factor is equal to zero, and on the other the GCSs represent to the LG modes when the phase factor is equal to $\pi/2$. It can be seen distinctly that HG modes steadily convert to LG modes by controlling the phase factor precisely. More importantly, the superposition of the GCSs with the particular phase factor reveals the patterns of experimental results: square pattern, hyperbolic pattern, elliptic pattern, and circular pattern. It is worthwhile to mention that the present GCSs are intimately correlated to the Ince-Gaussian (IG) beams described by Bandres and Gutierrez-Vega [25–28]. Ince-Gaussian beams not only constitute the exact and continuous transition modes between HG and LG beams but also constitute the third complete family of transverse eigenmodes of stable resonator. The transverse structures of IG modes are adjusted by the ellipticity factor, whereas the present GCSs are varied by the additional phase factor. It can be shown that IG modes can be completely identical to the GCSs with some connection between the ellipticity factor of IG modes and the phase factor of GCSs. However the representation of GCSs is more convenient and elegant to interpret the present experimental patterns.

We applied the GCSs to explain the experimental results and found that the observed vector patterns shown in Figs. 2(a)–2(d) can be fittingly described as following wave functions, respectively:

$$\vec{E}(x, y, z) = \Psi_{4,3}^{\sin}(x, y, z; 0.048\pi) \hat{x} + \Psi_{4,3}^{\cos}(x, y, z; 0.048\pi) \hat{y}, \quad (7)$$

$$\vec{E}(x, y, z) = \Psi_{5,13}^{\sin}(x, y, z; 0.305\pi) \hat{x} + [\Psi_{5,13}^{\cos}(x, y, z; 0.305\pi) - \Psi_{5,13}^{\sin}(x, y, z; 0.35\pi)] \hat{y}, \quad (8)$$

$$\vec{E}(x, y, z) = \Psi_{3,15}^{\sin}(x, y, z; 0.4\pi) \hat{x} + [\Psi_{3,15}^{\sin}(x, y, z; 0.295\pi) + \Psi_{2,17}^{\cos}(x, y, z; 0.295\pi)] \hat{y}, \quad (9)$$

$$\vec{E}(x, y, z) = \Psi_{0,21}^{\cos}(x, y, z; 0.48\pi) \hat{x} + \Psi_{0,21}^{\cos}(x, y, z; 0.45\pi) \hat{y}. \quad (10)$$

The wave function can be written as $\vec{E}(x, y, z) = \vec{E}_x(x, y, z) \hat{x} + \vec{E}_y(x, y, z) \hat{y}$, where $\vec{E}_x(x, y, z)$ and $\vec{E}_y(x, y, z)$ are composed by the GCSs. With the analytical function given in Eqs. (7)–(10), Fig. 8 depicts the numerically reconstructed patterns for the four kinds of the experimental results shown in Fig. 2. The patterns in Figs. 8(a) and 8(d) which are found to be close to HG and LG mode arise from the phase factor slightly different from the phase factor of HG and LG modes. Moreover, the superposition of GCSs with the phase factor appreciably different from the phase factors of HG and LG modes reveals the hyperbolic and elliptic modes shown in Figs. 8(b) and 8(c). From this point of view, the phase factor indeed plays a vital role in the GCSs to construct the polarization-entangled modes different from pure HG and LG modes.

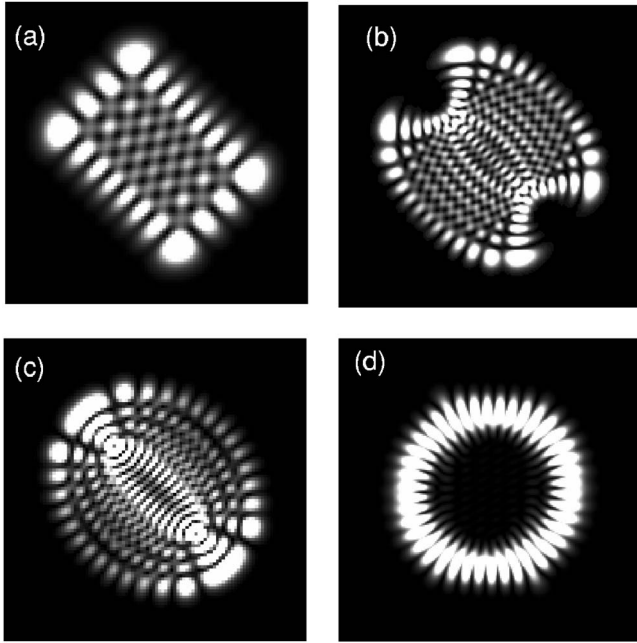


FIG. 8. Numerically reconstructed patterns for the experimental results shown in Fig. 2.

For stable stationary polarization-entangled wave patterns, the phase factor φ of the GCS is governed by the criterion of the maximum overlap between the cavity mode distribution and the pump distribution. Note that the maximum overlap integral corresponds to the minimum pump threshold. The overlap integral for the transverse mode $\vec{E}_i(x, y, z)$ can be written as

$$I(\varphi) = \iint S(x, y, z; \varphi) R_p(x, y) dx dy, \quad (11)$$

where the normalized intensity distribution $S(x, y, z; \varphi)$ and the pumping distribution $R_p(x, y)$ are given by

$$S(x, y, z; \varphi) = \frac{|\vec{E}_i(x, y, z)|^2}{\int_{-\infty}^{\infty} dx \int_{-\infty}^{\infty} dy \int_{-\infty}^{\infty} dz |\vec{E}_i(x, y, z)|^2}, \quad i = x, y \quad (12)$$

and

$$R_p(x, y) = \frac{2}{\pi} \frac{1}{\omega_p^2} \exp\left[-2 \frac{(x - x_0)^2 + (y - y_0)^2}{\omega_p^2}\right] \quad (13)$$

with the pumping radius $\omega_p \cong 25 \mu\text{m}$ in the scheme. Figure 9 shows the overlap functional $I(\varphi)$ as a function of φ for the state $\vec{E}_x = \Psi_{4,3}^{\sin}(x, y, z; \varphi)$ and $\vec{E}_x(x, y, z) = \Psi_{3,15}^{\sin}(x, y, z; \varphi)$ corresponding to the experimental patterns shown in Figs. 2(a) and 2(c) with $x_0 = -50 \mu\text{m}$, $y_0 = 63 \mu\text{m}$, and $x_0 = -137 \mu\text{m}$, $y_0 = 61 \mu\text{m}$, respectively. The maximum of the overlap indicates the most possible phase factor to construct the experimental result with the specific off axis. As a result, we can control the phase factor in the vicinity of the peaks 0.07π and 0.4π in Figs. 9(a) and 9(b) to simulate the patterns which

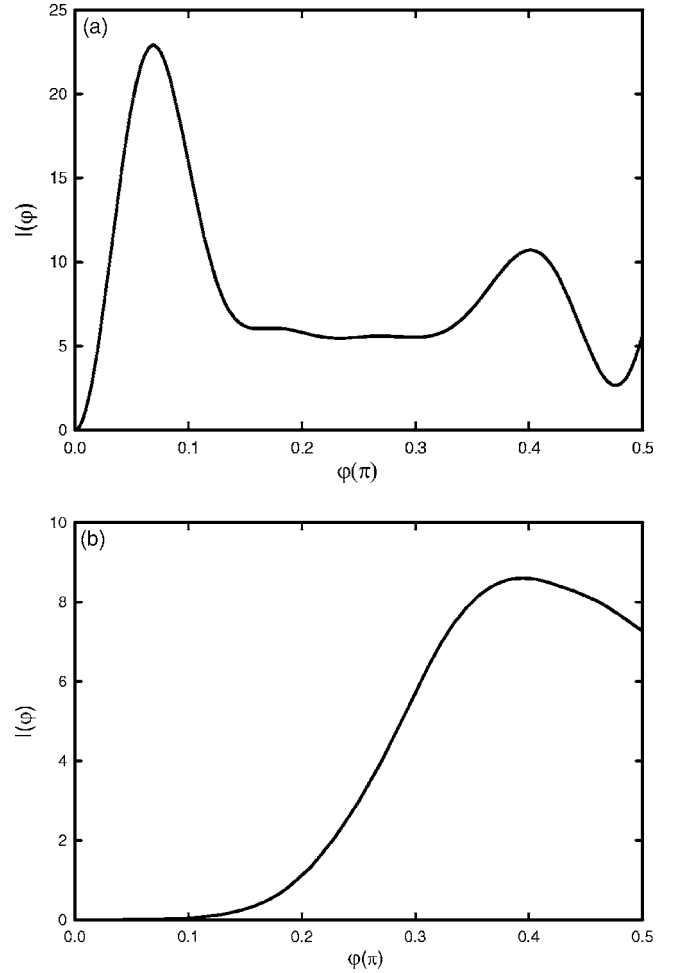


FIG. 9. (a) The overlap functional $I(\varphi)$ as a function of φ for the state $\vec{E}_x(x, y, z)$ in Eq. (7). (b) The overlap functional $I(\varphi)$ as a function of φ for the state $\vec{E}_x(x, y, z)$ in Eq. (9).

are in good agreement with the experimental patterns as shown in Figs. 2(a) and 2(c). The diagram of the phase factor indicates the accurate direction to construct the experimental results. In other words, we can manipulate various patterns by use of the relation between the pumping position and the phase factor in the overlap function. Continuously, Figs. 10–13 display the numerical results of the polarization-resolved patterns according to the patterns in Figs. 3–6. From the analytical results of the polarization-resolved patterns, we can confirm that the polarization-entangled patterns are composed of two distinct patterns with orthogonal linear polarization. The important point to note is that the transverse pattern is linearly polarized, but the polarization is spatially dependent. The good agreement between the reconstructed and experimental patterns verifies that the GCSs provide a practical description for the polarization-entangled optical coherent waves. Two types of point singularities in the polarization of a paraxial Gaussian laser beam had been researched in recent years. Vector singularities are isolated, stationary points in a plane at which the orientation of the electric vector of a linearly polarized vector field becomes undefined. Therefore elliptic singularities are isolated, stationary points in a plane at which the orientation of the el-

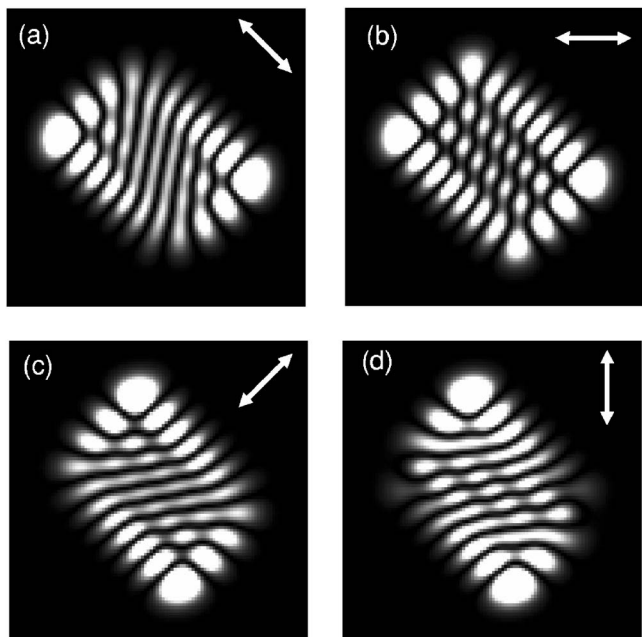


FIG. 10. Numerically reconstructed patterns for the experimental results shown in Fig. 3.

liptically polarized fields becomes undefined. In this paper, we investigate the elegant GCSs to reconstruct the polarization-entangled experimental results. For this reason, the V points of the various experimental patterns which are the transitions between HG and LG modes can be revealed explicitly. Vector point singularities are conventionally described in terms of the angle field $\Theta(x,y)=\arctan(E_y/E_x)$, where E_x and E_y are the scalar components of the vector field \vec{E} along the x and y axes. The vortices of $\Theta(x,y)$ are the vector singularities at which the orientation of the vector of \vec{E} is undefined. Figure 14 shows the contour plot of phase

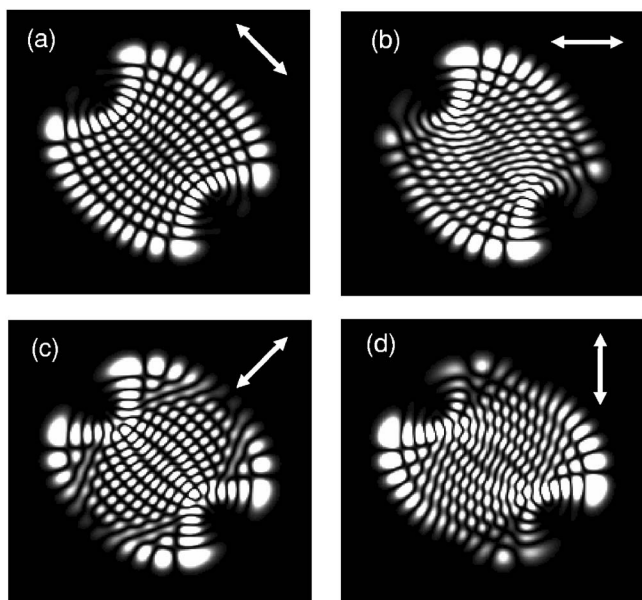


FIG. 11. Numerically reconstructed patterns for the experimental results shown in Fig. 4.

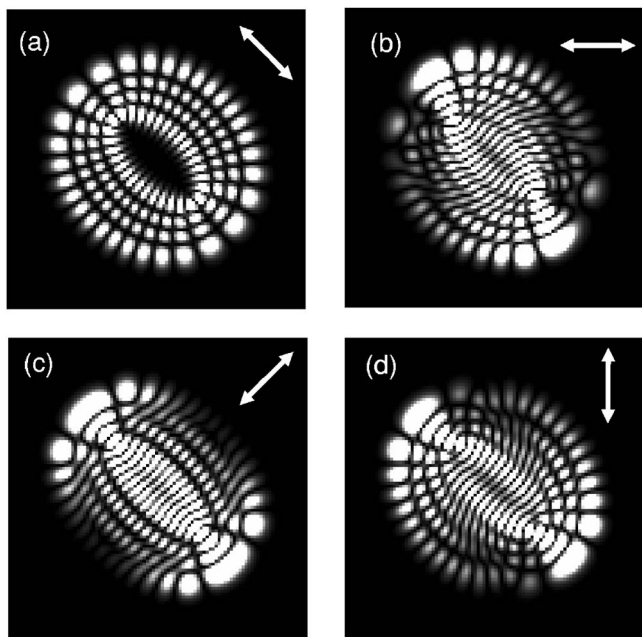


FIG. 12. Numerically reconstructed patterns for the experimental results shown in Fig. 5.

field $\Theta(x,y)$ according to the patterns which are reconstructed by the GCSs in Fig. 8. The contour plots reveal that the singularities of different GCSs belong to extremely different kinds of singular patterns. Figures 14(a), 14(b), and 14(d) display the grid, twist, and row patterns, respectively. As well, Fig. 14(c) shows that the singular pattern seems to be the transition between the twist and row patterns according to Figs. 14(b) and 14(d). Figure 15 depicts the contour plot of angle field $\Theta(x,y)$ for the boxed regions to show the details, and it can be found that all saddle points are to be

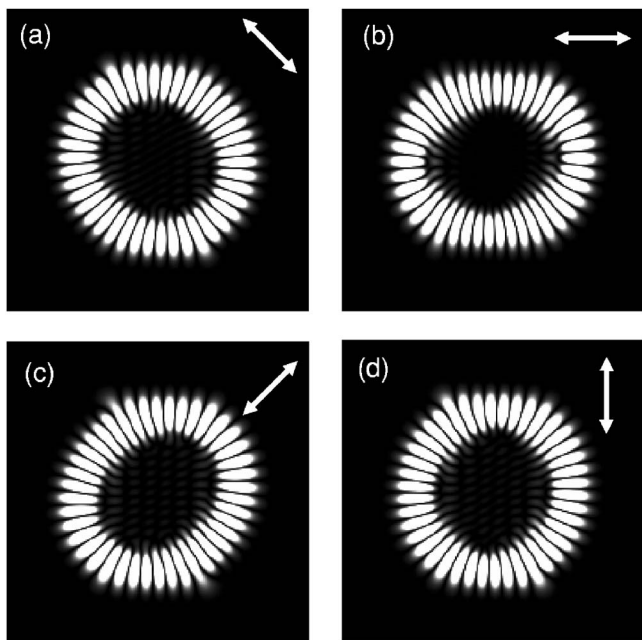


FIG. 13. Numerically reconstructed patterns for the experimental results shown in Fig. 6.

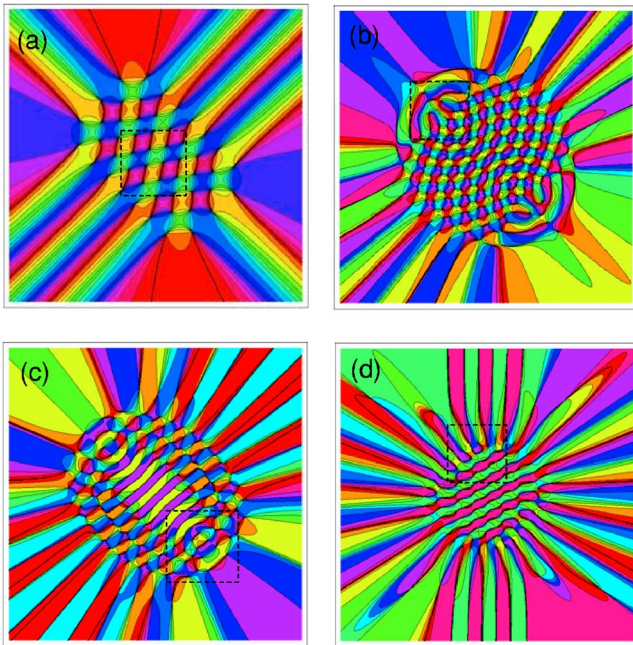


FIG. 14. (Color online) Contour plot of angle field $\Theta(x,y)$ according to the reconstructed patterns in Fig. 8.

open saddles with no joined arms. Since no closed saddles are found in the experimental vector field, no extrema are observed. As discussed in Refs. [29,30], the phase extrema are really rare because there is little room left in the phase field to accommodate them.

IV. CONCLUSION

In conclusion, we have used a high-level isotropic laser with off-axis focused pumping and on-axis defocused pumping to generate various high-order polarization-entangled optical coherent patterns. The structures of the polarization-entangled patterns are highly stable and the experimental results are easily reproducible. All the experimental patterns have been well analyzed with the GCSs which constitute a useful family of quantum states for the 2D harmonic oscilla-

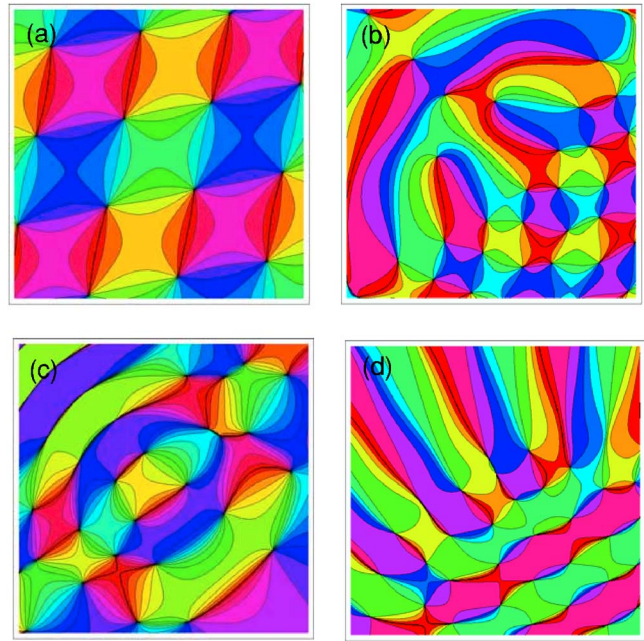


FIG. 15. (Color online) Contour plot of angle field $\Theta(x,y)$ for the boxed regions shown in Fig. 8.

tor. Furthermore, various patterns can be manifestly explained by use of the relation between the pumping position and the phase factor of the GCSs in the overlap integral. With the connection between theoretical analysis and experimental results, the formation of vector singularities can be clearly represented. The perfect reconstructed results also reveal that the GCSs play an important role in the mesoscopic region with optical coherent waves.

ACKNOWLEDGMENTS

The authors thank the National Science Council for their financial support of this research under Contract No. NSC-95-2112-M-009-041. This work is also supported in part by the MOE-ATU project.

-
- [1] K. F. Berggren, A. F. Sadreev, and A. A. Starikov, *Phys. Rev. E* **66**, 016218 (2002).
 [2] G. Blatter, M. V. Feigelman, and V. B. Geshkenbein, *Rev. Mod. Phys.* **66**, 1125 (1994).
 [3] R. E. Prange and M. Girvin, *The Quantum Hall Effect*, 2nd ed. (Springer-Verlag, Berlin, 1990).
 [4] *Optical Vortices*, edited by M. V. Vasnetsov and K. Staliunas (Nova Science, New York, 1999).
 [5] M. S. Soskin and M. V. Vasnetsov, in *Progress in Optics*, edited by E. Wolf (Elsevier, Amsterdam, 2001), Vol. 42, Chap. 4.
 [6] E. L. Andronikashvili and Y. G. Mamaladze, *Rev. Mod. Phys.* **38**, 567 (1996).
 [7] K. W. Madison, F. Chevy, W. Wohlleben, and J. Dalibard, *Phys. Rev. Lett.* **84**, 806 (2000).
 [8] J. F. Nye, *Proc. R. Soc. London, Ser. A* **387**, 105 (1983).
 [9] M. Soskin, V. Denisenko, and R. Egorov, *J. Opt. A, Pure Appl. Opt.* **6**, S281 (2004).
 [10] M. V. Berry, *J. Opt. A, Pure Appl. Opt.* **6**, 475 (2004).
 [11] I. Freund, *Opt. Commun.* **199**, 47 (2001).
 [12] L. Gil, *Phys. Rev. Lett.* **70**, 162 (1993).
 [13] T. Erdogan, *Appl. Phys. Lett.* **60**, 1921 (1992).
 [14] Y. F. Chen, K. F. Huang, H. C. Lai, and Y. P. Lan, *Phys. Rev. Lett.* **90**, 053904 (2003).
 [15] I. V. Veshneva, A. I. Konukhov, L. A. Melnikov, and M. V. Ryabinina, *J. Opt. B: Quantum Semiclassical Opt.* **3**, S209 (2001).

- [16] Y. F. Chen, Y. P. Lan, and K. F. Huang, *Phys. Rev. A* **68**, 043803 (2003).
- [17] Y. F. Chen, T. H. Lu, and K. F. Huang, *Phys. Rev. Lett.* **96**, 033901 (2006).
- [18] H. Kogelnik and T. Li, *Proceedings of the IEEE 54* (IEEE, Piscataway, 1966), pp. 1312–1329.
- [19] V. Bužek and T. Quang, *J. Opt. Soc. Am. B* **6**, 2447 (1989).
- [20] J. Banerji and G. S. Agarwal, *Opt. Express* **5**, 220 (1999).
- [21] Y. F. Chen and K. F. Huang, *Phys. Rev. E* **68**, 066207 (2003).
- [22] Y. F. Chen, Y. P. Lan, and K. F. Huang, *Phys. Rev. E* **66**, 066210 (2002).
- [23] Y. F. Chen and Y. P. Lan, *Phys. Rev. A* **66**, 053812 (2002).
- [24] Y. F. Chen and Y. P. Lan, *Phys. Rev. A* **67**, 043814 (2003).
- [25] Miguel A. Bandres and Julio C. Gutierrez-Vega, *Opt. Lett.* **29**, 2 (2004).
- [26] Ulrich T. Schwarz, Miguel A. Bandres, and Julio C. Gutierrez-Vega, *Opt. Lett.* **29**, 16 (2004).
- [27] Miguel A. Bandres, *Opt. Lett.* **29**, 15 (2004).
- [28] Miguel A. Bandres and Julio C. Gutierrez-Vega, *Opt. Lett.* **29**, 19 (2004).
- [29] I. Freund, *Phys. Rev. E* **52**, 2348 (1995).
- [30] M. S. Soskin, V. Denisenko, and I. Freund, *Opt. Lett.* **28**, 1475 (2003).